



Detection of diffusion anisotropy from an individual short particle trajectoryKaito Takanami ^{*}*Department of Physics, Graduate School of Science, The University of Tokyo, Tokyo 113-0033, Japan*Daisuke Taniguchi  and Masafumi Kuroda*International Research Center for Neurointelligence (WPI-IRCN), The University of Tokyo, Tokyo 113-0033, Japan
and Laboratory for Cell Polarity Regulation, RIKEN Center for Biosystems Dynamics Research (BDR), Osaka 565-0874, Japan*

Sawako Enoki

*Universal Biology Institute (UBI), The University of Tokyo, Tokyo 113-0033, Japan
and Laboratory for Cell Polarity Regulation, RIKEN Center for Biosystems Dynamics Research (BDR), Osaka 565-0874, Japan*Yasushi Okada *Department of Physics, Graduate School of Science, The University of Tokyo, Tokyo 113-0033, Japan;
International Research Center for Neurointelligence (WPI-IRCN), The University of Tokyo, Tokyo 113-0033, Japan;
Department of Cell Biology, Graduate School of Medicine, The University of Tokyo, Tokyo 113-0033, Japan;
Universal Biology Institute (UBI), The University of Tokyo, Tokyo 113-0033, Japan;
and Laboratory for Cell Polarity Regulation, RIKEN Center for Biosystems Dynamics Research (BDR), Osaka 565-0874, Japan*Yoshiyuki Kabashima [†]*Department of Physics, Graduate School of Science, The University of Tokyo, Tokyo 113-0033, Japan;
The Institute for Physics of Intelligence, The University of Tokyo, Tokyo 113-0033, Japan;
and Trans-Scale Quantum Science Institute, The University of Tokyo, Tokyo 113-0033, Japan*

(Received 23 May 2024; accepted 19 August 2024; published 9 September 2024)

In parallel with advances in microscale imaging techniques, the fields of biology and materials science have focused on precisely extracting particle properties based on their diffusion behavior. Although the majority of real-world particles exhibit anisotropy, their behavior has been studied less than that of isotropic particles. In this study, we introduce a method for estimating the diffusion coefficients of individual anisotropic particles using short-trajectory data on the basis of a maximum likelihood framework. Traditional estimation techniques often use mean-squared displacement (MSD) values or other statistical measures that inherently remove angular information. Instead, we treated the angle as a latent variable and used belief propagation to estimate it while maximizing the likelihood using the expectation-maximization algorithm. Compared to conventional methods, this approach facilitates better estimation of shorter trajectories and faster rotations, as confirmed by numerical simulations and experimental data involving bacteria and quantum rods. Additionally, we performed an analytical investigation of the limits of detectability of anisotropy and provided guidelines for the experimental design. In addition to serving as a powerful tool for analyzing complex systems, the proposed method will pave the way for applying maximum likelihood methods to more complex diffusion phenomena.

DOI: [10.1103/PhysRevResearch.6.033272](https://doi.org/10.1103/PhysRevResearch.6.033272)**I. INTRODUCTION**

Advances in imaging techniques have made it possible to visualize the spatiotemporal dynamics of various materials in

microscale. This has sparked the development of theoretical methods for quantitatively extracting the physical properties of materials from experimental data. Among these methods, analyzing the mobility of a single tracer particle immersed in viscoelastic material has emerged as a powerful technique to reveal the microenvironment of the materials [1]. To date, this technique has been widely applied to elucidate the dynamics and structure of cell membranes [2–4], DNA synthesis [5,6], principles of protein transport [7–9], and even the processes and infection mechanisms of viruses [10,11].

Conventionally, this technique often assumes the use of spherical tracer particles [12] or nonrotational tracer particles [13] for ease of statistical analysis. In other words, the

^{*}Contact author: takanami255@g.ecc.u-tokyo.ac.jp[†]Contact author: kaba@phys.s.u-tokyo.ac.jp

Published by the American Physical Society under the terms of the [Creative Commons Attribution 4.0 International](https://creativecommons.org/licenses/by/4.0/) license. Further distribution of this work must maintain attribution to the author(s) and the published article's title, journal citation, and DOI.

difficulty of statistical analysis has prevented the application of this method to complex materials such as biological samples, where tracer particles generally have nonspherical shapes. However, recent biological studies have revealed the numerous characteristics and roles of anisotropic particles [14–18]. For example, their unique shapes and properties have been shown to be useful in drug delivery [19–21] and in the control of critical phenomena in active matter [22]. This had led to a growing interest in the potential and versatility of anisotropic particles in biological research.

Although the physics on anisotropic diffusion has been intensively explored since some pioneering studies [23–25], to date, only a few data-analysis methods have been proposed to address the trajectories of nonspherical tracer particles [26–30]. These methods often require an unrealistically large number of time points in a single trajectory or the averaging of a large number of multiple trajectories. Moreover, some studies have assumed that the orientation of anisotropic particles can be observed [31]. However, this assumption is often invalid, especially when the particles are very small.

Taking these circumstances into consideration, this study addresses the practical problem of estimating the diffusion coefficients of a two-dimensional anisotropic particle from single-particle tracking (SPT) data. To this end, we employed the stochastic model of anisotropic diffusion introduced in Ref. [26].

It is important to note that this two-dimensional model is a simplification of three-dimensional reality. In a full three-dimensional treatment, one would need to consider movement along the z axis and introduce a second angle to completely describe the particle's orientation. However, for many practical applications this two-dimensional approximation provides valuable insights while maintaining computational tractability. For example, we consider the tracer movement in shallow chambers in vitro, around cell periphery (lamellipodia), and with the regions beneath nuclei, which are not unusual cases in microscopy observations. In these situations, the depth of field is often on the order of submicron scales, and translational and rotational movements in the z direction are constrained, allowing the system to be effectively treated as quasi two-dimensional. This consistency with real-world conditions forms a significant part of our motivation for employing this model.

Consider a two-dimensional particle with different translational diffusion coefficients $D_a > D_b$, which correspond to the major and minor axis directions, respectively. In addition, let D_θ be the rotational diffusion coefficient of the particle. The dynamics of the center-of-mass position coordinates x , y and angles θ of a single particle are described by the following Langevin equation:

$$\frac{\partial x}{\partial t} = \xi_1(t) \quad \frac{\partial y}{\partial t} = \xi_2(t) \quad \frac{\partial \theta}{\partial t} = \xi_3(t). \quad (1)$$

Here, $\xi_1(t)$, $\xi_2(t)$, and $\xi_3(t)$ are Gaussian white noise characterized by $\langle \xi_i(t) \rangle = \langle \xi_j(t) \rangle = \langle \xi_3(t) \rangle = 0$ and

$$\begin{aligned} \langle \xi_i(t) \xi_j(t') \rangle &= \Sigma_{ij} \delta(t - t') \quad (i, j = 1, 2) \\ \langle \xi_3(t) \xi_3(t') \rangle &= 2D_\theta \delta(t - t'), \end{aligned}$$

where Σ denotes

$$\Sigma(\theta) = \begin{pmatrix} (2\bar{D} + \Delta D \cos 2\theta) & \Delta D \sin 2\theta \\ \Delta D \sin 2\theta & 2\bar{D} - \Delta D \cos 2\theta \end{pmatrix}$$

with $\bar{D} = (D_a + D_b)/2$ and $\Delta D = D_a - D_b$. Brackets represent the average with respect to $\xi_1(t)$, $\xi_2(t)$, and $\xi_3(t)$. Furthermore, when Gaussian observation noise is added to each coordinate, the observed coordinates X , Y are given by $X(t) = x(t) + \epsilon \xi_4(t)$ and $Y(t) = y(t) + \epsilon \xi_5(t)$, where ϵ is the standard deviation of the noise magnitude, and $\xi_4(t)$ and $\xi_5(t)$ represent independent standard Gaussian white noise. Using these notations, we aim to precisely estimate the diffusion coefficients D_a , D_b , and D_θ from a pair of observed time series, $\mathbf{X}, \mathbf{Y} = \{\mathbf{X}(\mathbf{t}_i), \mathbf{Y}(\mathbf{t}_i)\}_{1 \leq i \leq N}$, with a time interval Δt . Note that we consider a general situation in which the orientation of the particles cannot be observed and must be inferred. Mean-squared displacement is a classical approach that is still the most commonly used technique to estimate diffusion coefficients (MSD) [32–36]. Two well-known methods are used for applying MSD fitting to particle trajectories obtained by SPT [35]: one is a trajectory-segmentation method that allows overlap, and the other is a method that extracts trajectories independently without allowing overlap. However, in two-dimensional anisotropic diffusion, anisotropy does not appear in the MSD; therefore, the statistical nature of diffusion must be examined using the fourth-order cumulant to detect anisotropy [26]. As shown by Ref. [26], when the particle orientation is hidden with no measurement noise, the MSD and fourth-order cumulant are given by

$$D_{xx}(t) = D_{yy}(t) = \bar{D} \quad (2)$$

$$C_4(t) = \frac{3\Delta D^2}{4D_\theta} \left(t - \frac{1 - \exp(-4D_\theta t)}{4D_\theta} \right). \quad (3)$$

When the three diffusion coefficients are estimated using a fourth-order cumulant, two parameters must be estimated from a single equation, because D_θ and ΔD are coupled in Eq. (3). In addition, in the $D_\theta \rightarrow \infty$ limit, the fourth-order cumulant vanishes regardless of time, and estimating ΔD and D_θ from the fourth-order cumulant is, in principle, impossible regardless of the length of each particle trajectory. Another drawback is that it does not use the full microscopic diffusion information contained in the time series.

To address these limitations, we developed a method based on maximum likelihood estimation (MLE) for analyzing the mobility of anisotropic particles from the data of only single and short trajectories (Fig. 1). Traditional fitting methods tend to lose information at higher moments. However, the MLE method efficiently exploits the information, including those with higher moments, from the data by maximizing the likelihood of the entire trajectory. The maximization is implemented using the expectation-maximization (EM) algorithm [37] to incorporate latent variables. In the current system, belief propagation (BP) [38] enables the algorithm to operate linearly with respect to the number of data points. However, in practice, BP is not feasible to perform analytically because it is expressed as a set of functional recurrence formulas. As a practical solution to this problem, we use particle-filter (sequential Monte Carlo) methods [39,40].

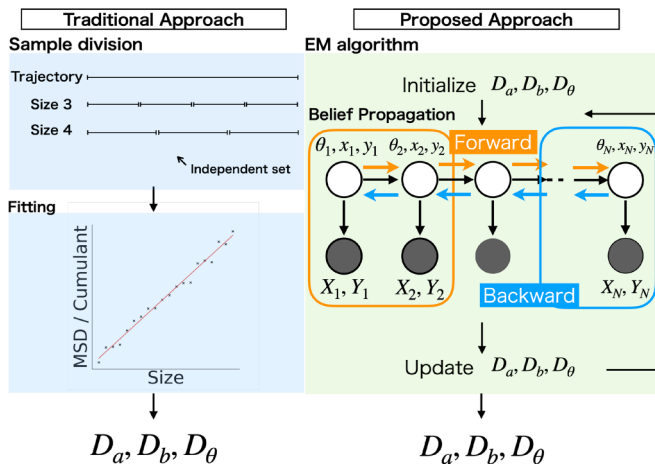


FIG. 1. Illustration of the traditional fitting approach and the proposed MLE approach. In the fitting approach, a single trajectory is segmented to multiple paths of varying lengths, from which the MSD and relevant cumulants are computed. In the MLE approach, on the other hand, given the initial values, the diffusion coefficients are recursively updated by the EM algorithm based on relevant moments of latent variables with respect to the posterior distribution defined by the diffusion coefficients at the time. The moment assessment is efficiently performed by BP, which is implemented by particle filters.

The usefulness of our approach was validated by performing numerical studies and laboratory experiments using bacteria, quantum rods, and fluorescent spheres. We found that compared to conventional statistical methods widely used for estimating diffusion coefficients, our method can detect anisotropy more sensitively and estimate the diffusion coefficients of nonspherical tracer particles using shorter trajectories.

Additionally, we analytically explored the detection limit of anisotropy. Similarly to the discussion in Ref. [41], which addressed the reliability of the MLE in the isotropic model, we quantitatively evaluated the distribution of maximum likelihood values in cases where anisotropy is present. Our method employs fixed-point analysis of the EM algorithm, examining instances where the finiteness of paths could potentially lead to erroneous detection of isotropy. This analysis reveals that, due to the finite nature of the length of trajectories, the limitations of the MLE method can result in false conclusions with a certain probability. These findings contribute to enhancing the robustness of experimental designs and data interpretation in this challenging area of research, providing experimental guidelines concerning the required length of trajectories and the acceptable magnitude of measurement noise.

II. RESULTS

A. Numerical studies

Figure 2 presents the diffusion coefficients estimated from trajectories generated by numerical simulations with known diffusion coefficients. The simulations were conducted using four different parameter sets. The experimental procedure was as follows: First, we set the true diffusion coefficients and generated trajectories using numerical simulations according to Eq. (1). We then masked the angles and true position

coordinates, treating them as unknown, and performed estimations using only the noise-added coordinates. For the MSD method, we calculated the MSD and fourth-order cumulants from the trajectories. Taking noise into account, we estimated the diffusion coefficients by fitting using Eqs. (2) and (3). For the MLE method, we employed the EM algorithm, which will be described in detail later.

As a result, in all cases, the MLE method outperformed conventional cumulant-based fitting. The fitting method achieved some degree of success in estimating D_a and D_b only when the rotational diffusion coefficient was small, that is, $\sqrt{2D_\theta \Delta t} < 1$ [Figs. 2(a) and 2(b)]. However, the MLE method succeeded in estimating both D_a and D_b with higher precision, even for shorter trajectories. Moreover, the MLE method could accurately estimate the correct order of magnitude for D_θ even for trajectories as short as $N = 100$, which is impossible to achieve using the fitting method.

In more challenging scenarios where $\sqrt{2D_\theta \Delta t} > 1$ [Figs. 2(c) and 2(d)], the fitting method completely failed to estimate D_a and D_b . In particular, Fig. 2(c) shows an erroneous estimation of $D_b = 0$, and Fig. 2(d) represents an incorrect conclusion of $D_a = D_b$. This failure is attributable to the fact that the fourth-order cumulant Eq. (3) vanishes asymptotically as D_θ increases, thereby making the fitting process highly challenging. In particular, in Fig. 2(d), distinguishing between isotropic and anisotropic diffusion becomes exceedingly difficult. Nonetheless, the MLE method successfully estimates D_a and D_b with high accuracy in both cases, and also successfully detects anisotropy.

We found that the fourth-order cumulant is not useful for determining ΔD and D_θ because it exhibits significant statistical errors (Fig. 3 in the large t regimes). This leads to practical difficulties in accurately estimating ΔD and D_θ . In particular, when D_θ is large, $C_4(t)$ does not respond to variations in ΔD , which results in complete failure of the estimation, as shown in Fig. 3(a). Moreover, as D_θ decreases, the cumulant method fails to predict even the correct order of D_θ , as shown in Fig. 3(b).

As verified in Figs. 2(a) and 2(b), our method can estimate not only the translational diffusion coefficients D_a and D_b but also the rotational diffusion coefficient D_θ , even though the angle θ is hidden. However, Figs. 2(c) and 2(d) also show that if $\sqrt{2D_\theta \Delta t} > 1$, the estimation error of D_θ increases, because the angles are determined almost independently at each time step. To clarify this phenomenon further, Fig. 4 shows the landscape of the likelihood function for the true value of D_θ . When the rotational diffusion coefficient is too small ($\sqrt{2D_\theta \Delta t} \ll 1$), the likelihood function lacks extrema, making it impossible to estimate its order [Fig. 4(a)]. This can be attributed to the effect of measurement noise, which becomes significant owing to the absence of angular observations. Conversely, when the rotational diffusion coefficient is large ($\sqrt{2D_\theta \Delta t} > 1$), the $\pm\pi$ periodicity of the angles causes the likelihood function to lack extrema [Figs. 4(e) and 4(f)]. Therefore, as for the angular diffusion, our method may be effective only when the true D_θ has a moderate value. Nevertheless, even when accurate estimation of the order of the rotational diffusion coefficient is not possible, the translational diffusion coefficients can still be accurately estimated. Finally, one point that requires consideration is that this is not a

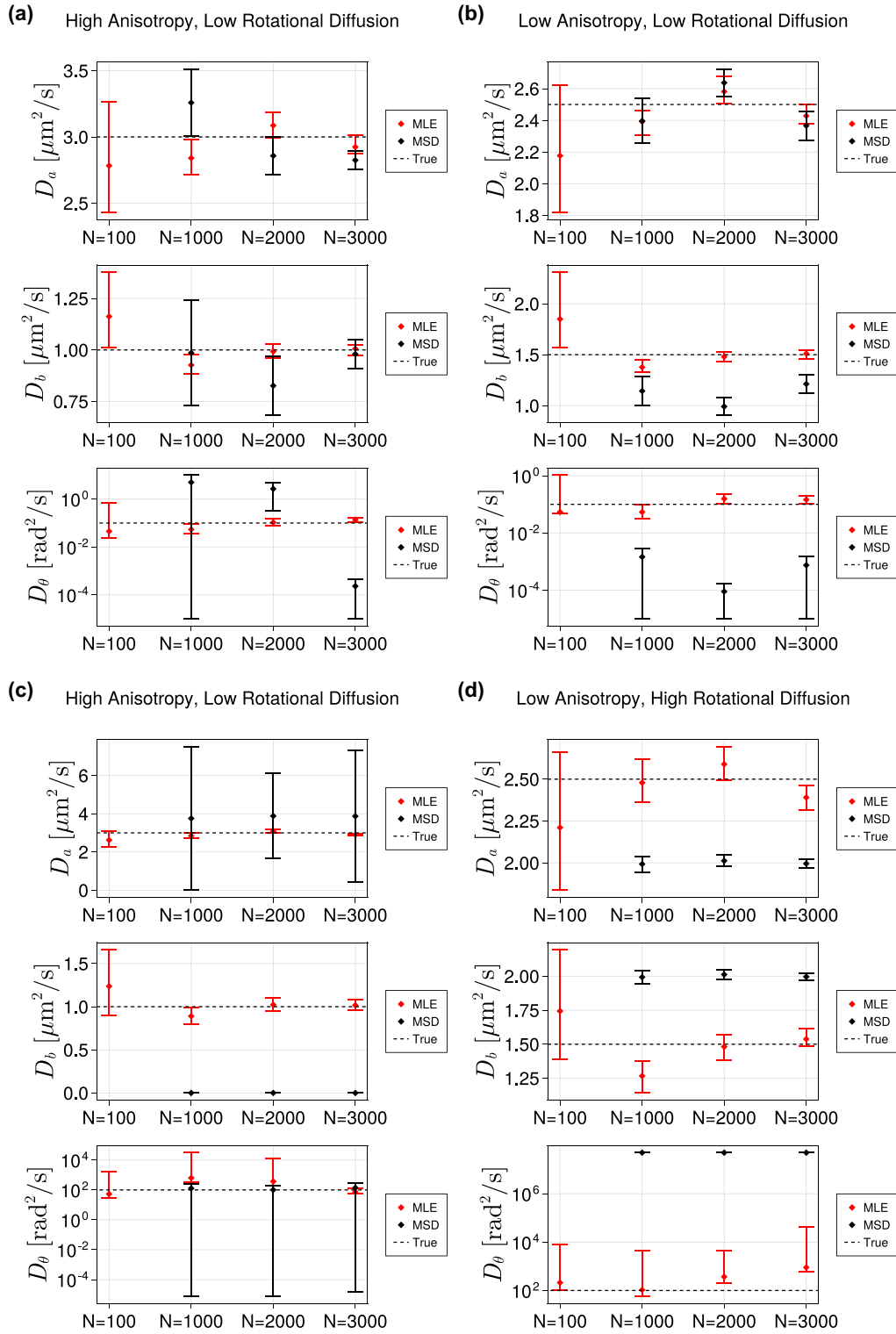


FIG. 2. Results of simulations performed using the MLE method compared to those performed using the fitting method. Experiments were conducted with four different parameter sets. The results of the fitting method for $N = 100$ are omitted because the error bars are too large and the estimation accuracy is obviously bad. Plots of D_θ are shown in log scale. The error bars represent the $\pm 1\sigma$ range obtained by Gaussian approximation of the likelihood function on either side of the maximum likelihood estimate. (a) $D_a = 3.0 \mu\text{m}^2/\text{s}$, $D_b = 1.0 \mu\text{m}^2/\text{s}$, $D_\theta = 0.1 \text{rad}^2 \text{s}^{-1}$. (b) $D_a = 2.5 \mu\text{m}^2/\text{s}$, $D_b = 1.5 \mu\text{m}^2/\text{s}$, $D_\theta = 0.1 \text{rad}^2 \text{s}^{-1}$. (c) $D_a = 3.0 \mu\text{m}^2/\text{s}$, $D_b = 1.0 \mu\text{m}^2/\text{s}$, $D_\theta = 100 \text{rad}^2 \text{s}^{-1}$. (d) $D_a = 2.5 \mu\text{m}^2/\text{s}$, $D_b = 1.5 \mu\text{m}^2/\text{s}$, $D_\theta = 100 \text{rad}^2 \text{s}^{-1}$ (a)–(d) $\Delta t = 0.01 \text{ s}$, $\epsilon = 0.02 \mu\text{m}$.

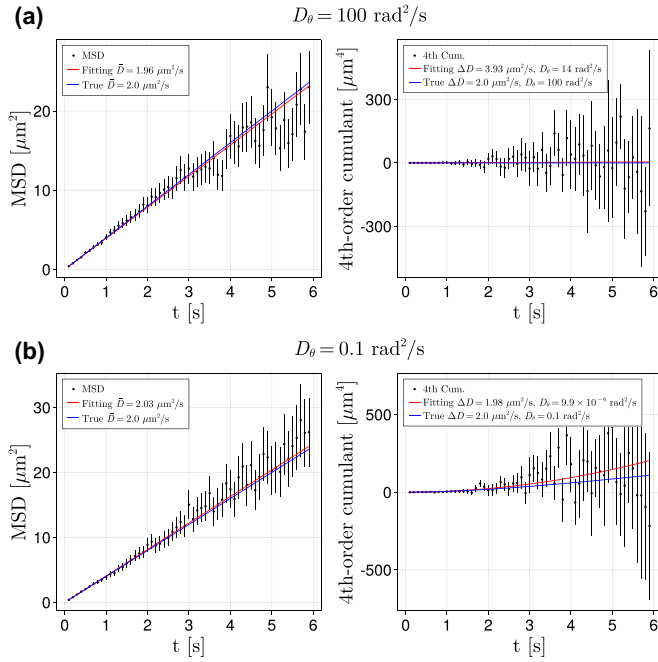


FIG. 3. MSD and the fourth-cumulant estimated by fitting to simulation data. (a) and (b) $D_a = 3.0 \mu\text{m}^2 \text{ s}^{-1}$, $D_b = 1.0 \mu\text{m}^2 \text{ s}^{-1}$, $\Delta t = 0.01 \text{ s}$, $\epsilon = 0.02 \mu\text{m}$, $N = 3000$. (A) $D_\theta = 100.0 \text{ rad}^2 \text{ s}^{-1}$. Error bars represent $\langle \Delta x(t)^2 + \Delta y(t)^2 \rangle / \sqrt{2n}$. (b) $D_\theta = 0.1 \text{ rad}^2 \text{ s}^{-1}$. Error bars stand for $\sqrt{6}([\Delta x(t)^2 + \Delta y(t)^2]^2) / \sqrt{4n}$. For both cases, n is the number of simulations (see Supplemental Material [42]).

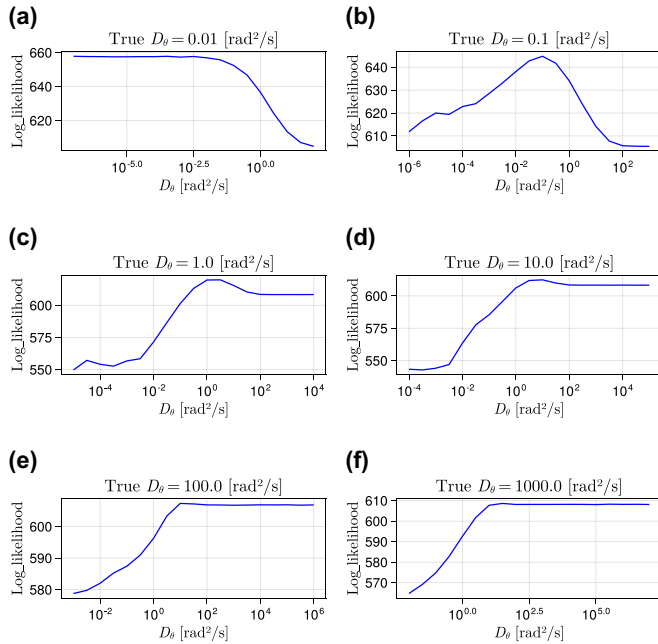


FIG. 4. Log likelihood vs D_θ when D_a and D_b are fixed to their true values. (a) When the true value of D_θ is too small, distinguishing the influence of measurement noise from that of the rotational diffusion is difficult, making the true value indistinguishable from smaller values of D_θ . (b and c) The correct order of D_θ can be estimated only when the true value of D_θ is moderate. (d)–(f) Conversely, when the true D_θ is too large, due to the $\pm\pi$ periodicity of the angle variables, distinguishing it from larger values is difficult. (a)–(f) $D_a = 2.0 \mu\text{m}^2/\text{s}$, $D_b = 1.0 \mu\text{m}^2/\text{s}$, $\Delta t = 0.01 \text{ s}$, and $\epsilon = 0.02 \mu\text{m}$.

discussion of the practical performance of the estimation algorithm, but instead concerns the general estimability with respect to the likelihood function.

B. Application to biological systems

The numerical results in the previous section confirm that our MLE-based method significantly outperforms conventional cumulant-based methods for a wide range of diffusion coefficients. To verify the utility of this method for real biological samples, we estimated the diffusion coefficients of micron-sized bacterial cells in quasi-two-dimensional suspensions confined between two parallel glass walls [Fig. 5(a)]. First, we extracted trajectory segments of $N = 3000$ length from four independent datasets, partitioned them into six $N = 500$ subsets, and estimated the diffusion coefficients for each. The results were compared with the estimates using the full $N = 3000$ dataset. Interestingly, for Data2 and Data3, the estimated diffusion coefficients did not vary significantly across the subsets. In contrast, for Data1 and Data4, the translational diffusion coefficients appeared to particularly differ across subsets. While this may be attributed to fluctuations in the distance between the bacteria and chamber walls [43], the salient point is that the MLE method can detect such time-dependent variations in the diffusion coefficients even over short intervals. This indicates the potential of the method to identify nonstationary particle behaviors during diffusion from short-length trajectories.

Micron-sized bacteria clearly show nonzero asphericity [44] ~ 0.72 in their trajectories [Fig. 5(b) left column], an evidence that the bacteria are spherically asymmetric. Furthermore, micron-sized bacteria allow for angle observations, which enable the verification of agreement between the estimated angles and actual observations. Figure 5(b) right column compares the estimated angular distributions $p(\theta | \mathbf{X}, \mathbf{Y}, \mathbf{D}^*)$ with the actual observations, where \mathbf{D}^* represents the estimated diffusion coefficients. Although we did not utilize any angular observation information to derive $p(\theta | \mathbf{X}, \mathbf{Y}, \mathbf{D}^*)$, Fig. 5(b) shows a good agreement between the estimated and observed bacterial angles. Thus, even when the particles are too small for directional detection, the directional behavior can still be estimated with high precision from noise-added trajectories alone as a simultaneous outcome of diffusion coefficient estimation.

C. Application to nanosized anisotropic particles

Owing to the slow rotational diffusion and pronounced anisotropy of micron-sized bacteria [Fig. 5(b)], detecting diffusion anisotropy in these bacteria is relatively easy. To further validate the effectiveness of our approach, we examined more challenging nanosized systems, namely, the diffusion of quantum rods and fluorescent spheres, which exhibit lesser anisotropy and faster rotational diffusion. Figure 6(a) shows the estimated translational diffusion coefficients for 19 independent trajectories of the quantum rods. The conventional fitting approach tended to either incorrectly infer isotropic behavior ($D_a = D_b$) or produce extreme parameters, such as $D_b = 0$. This can be attributed to a failure in fitting the fourth-order cumulant, which yielded erroneous

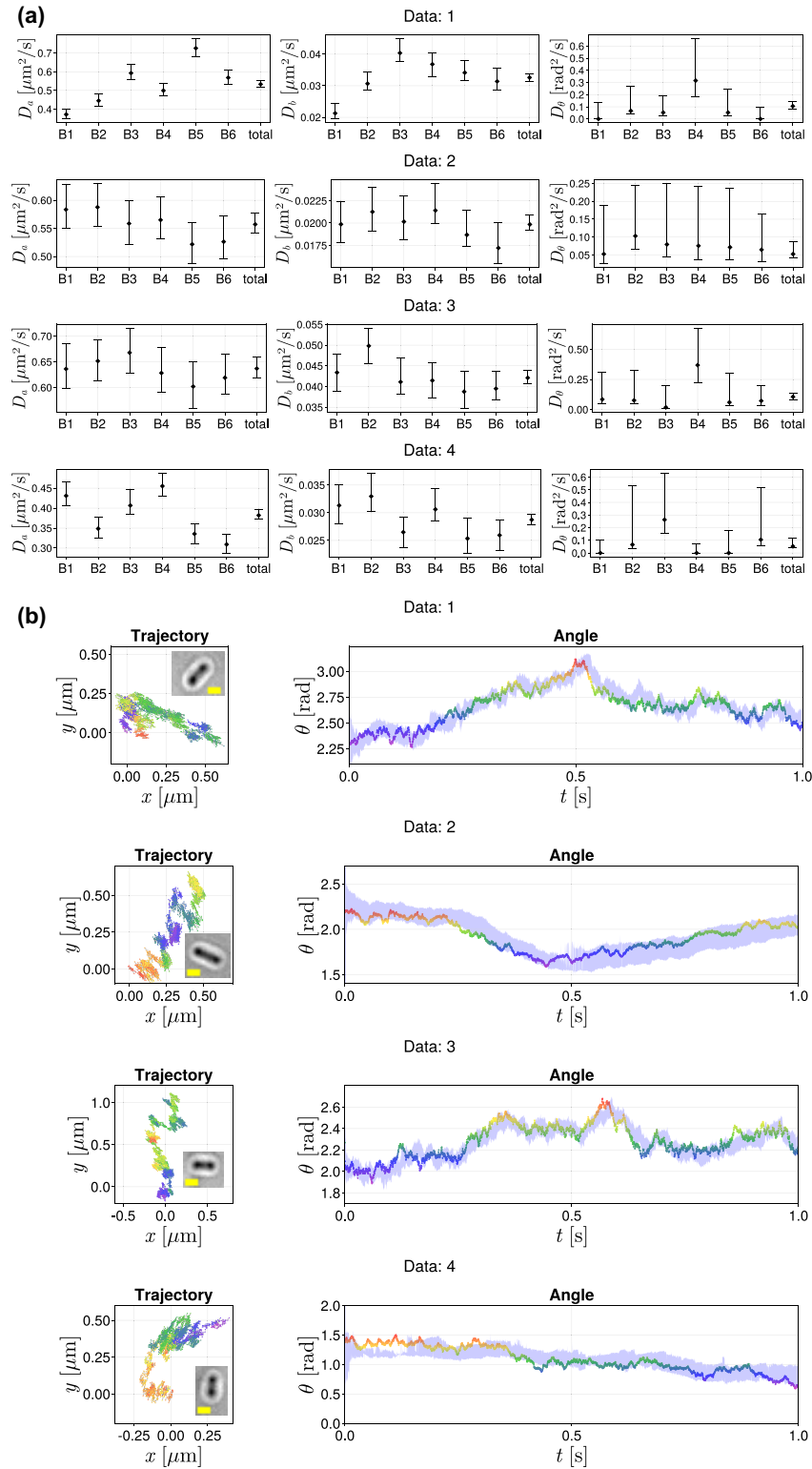


FIG. 5. Results obtained by the MLE method for four diffusion trajectories of bacteria. (a) The results obtained by dividing the $N = 3000$ trajectory into six subsets and estimating the diffusion coefficients in each $N = 500$ block are compared to the result obtained from the whole $N = 3000$ data. The error bars represent the $\pm 1\sigma$ range obtained by Gaussian approximation of the log-likelihood function on either side of the maximum likelihood estimate. (b) Actual trajectories (left column) and estimated angles (right column). The inset in each trajectory data shows a snapshot of a bacterium with a yellow scale bar ($1\ \mu\text{m}$). The angles at each time point are color coded. The blue bands indicate the 90% confidence intervals of the estimated angles. (a) and (b) $\Delta t = 0.33\ \text{ms}$ and $\epsilon = 0.00395\ \mu\text{m}$. The measurement error ϵ was estimated as the positional standard deviation of the bacteria immobilized on the glass wall.

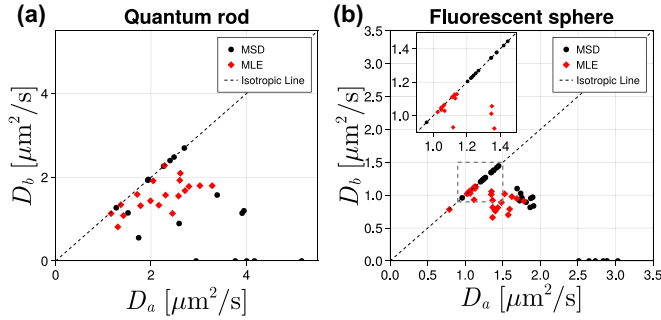


FIG. 6. Results obtained by the MLE method for the diffusion trajectories of (a) quantum rods and (b) fluorescent spheres. The nominal major and minor axis lengths of the quantum rod are 28.4 ± 3.0 and 4.6 ± 0.7 nm, respectively. The nominal diameter of the fluorescent spheres is 200 nm. (a) and (b) $N = 1000$, $\Delta t = 0.01$ s and $\epsilon = 0.02 \mu\text{m}$. The measurement error ϵ was estimated as the positional standard deviation of the immobilized tracers.

estimations that fall into the extremities of the parameter space, such as $\Delta D = 0$ or $\Delta D = D_a$. Conversely, the estimates obtained using our method eliminate extreme solutions such as $D_b = 0$ and reduce the fraction of trajectories classified as isotropic. This suggests that our method can detect anisotropy with high accuracy even in trajectories exhibiting very low non-Gaussianity, where the fourth-order cumulant approaches zero. However, some data were still classified incorrectly as isotropic.

D. Application to nanosized isotropic particles

Our method was originally formulated to detect diffusion anisotropy, but can also handle isotropic diffusion in the limit case of $D_a = D_b$. To confirm the detection performance for isotropic diffusion, we used the trajectories of fluorescent spheres to estimate the diffusion coefficients [Fig. 6(b)]. Almost half of the 28 trajectories were classified as isotropic, which is consistent with the theoretical probability of detecting diffusion isotropy, the details of which are discussed in the next section [Fig. 7(a)].

E. Stability analysis of the EM algorithm

The results in Fig. 6(a) [6(b)] suggest that several trajectories can lead to incorrect isotropic (anisotropic) estimation outcomes, even using our MLE method when D_θ is sufficiently large. To investigate the reason for this, we theoretically analyzed the dynamic behavior of the EM algorithm. Because of the symmetry between D_a and D_b , an isotropic fixed point always exists in the EM algorithm. To examine whether an isotropic fixed point is preferable, we linearized the EM algorithm around this point and examined the resulting stability matrix. This yielded the eigenvalue q corresponding to the eigenvector that breaks the isotropy as follows:

$$q = 1 + \left(\frac{D_a - D_b}{D_a + D_b} \right)^2 \left(\frac{1}{e^{4D_\theta \Delta t} - 1} + \frac{1}{2} \right) \quad (4)$$

in the $N \rightarrow \infty$ limit and $\epsilon = 0$. The derivation is provided in the Supplemental Material [42]. This result implies that it

always exceeds 1 as long as $D_a \neq D_b$; that is, if the particle is anisotropic, the isotropic fixed point is unstable. Therefore, anisotropic particle properties can always be detected if an infinitely long trajectory is observable without measurement noise even if $D_\theta \rightarrow \infty$. The reason for this counterintuitive conclusion is that in Eq. (3), D_θ and ΔD are completely coupled, such that the fourth-order cumulant converges to zero when D_θ is infinite, whereas in Eq. (4), there exists a term in which ΔD and D_θ are decoupled by the term $+1/2$. This decoupling term remains even if $D_\theta \rightarrow \infty$, enabling the detection of diffusion anisotropy.

Nevertheless, in realistic situations, the length of the observable trajectory is finite and measurement noise is inevitable. Under these conditions, the results described by Eq. (4) no longer hold, and the eigenvalues may dip below unity, depending on the statistical fluctuations of the sampled trajectory. In other words, even if the particle is nonspherical, the observed trajectory may display isotropic characteristics by chance, making the isotropic solution locally optimal. (Note that this is actually globally optimal in most cases; see Supplemental Material [42]). Figure 7(a) illustrates the probability of observing a trajectory with an eigenvalue q greater than 1 and summarizes the dependency of this probability on N , ϵ , D_a , and D_b . As expected, this figure shows that the larger the difference in the diffusion coefficient ΔD , the higher the probability of successful anisotropy detection.

We also introduced ΔD^* as the minimum ΔD value with a 75% probability of an eigenvalue exceeding 1 on the line of $D_a \Delta t + D_b \Delta t = 10.0 \mu\text{m}^2$, which serves as the detection threshold for anisotropy. Using ΔD^* , we first revealed that the probability of the eigenvalues exceeding 1 asymptotically approaches 100% within the limit of an infinitely large number of observations (Fig. 7). This result indicates that our method reliably detects anisotropy even in the presence of observation noise within the limit of $N \rightarrow \infty$. Second, we found that the threshold ΔD^* decreased with $\mathcal{O}(N^{-1/4})$ with respect to the trajectory length N and that the order is almost independent of noise [Fig. 7(b)]. This result demonstrates that the estimation accuracy depends moderately on the trajectory length. Finally, we verified that the amplitude of the measurement noise has little effect on the probability of detecting anisotropy when $\epsilon < \epsilon^*$, where ϵ^* corresponds to a diffusion signal-to-noise ratio of 1, that is, $\epsilon^* = \sqrt{2\bar{D}\Delta t}$. In contrast, we found that the amplitude of the measurement noise has a substantial effect on the probability of detecting anisotropy when the magnitude of noise exceeds the typical magnitude of diffusion ($\epsilon > \epsilon^*$) [Fig. 7(c)].

These results can be used to assess the number of observations and noise level required to reliably detect anisotropy. Specifically, by performing the numerical simulations used to create Fig. 7, we can evaluate N and ϵ required to achieve an acceptable level of success probability of anisotropy detection for each estimation result. Furthermore, Fig. 7 also offers qualitative guidance for improving the performance of anisotropy detection: Increasing the number of observations is more effective than reducing the measurement noise when the noise is smaller than ϵ^* . We remark that this result is not specific to the EM algorithm because it relates to the landscape of the likelihood function and is algorithm independent

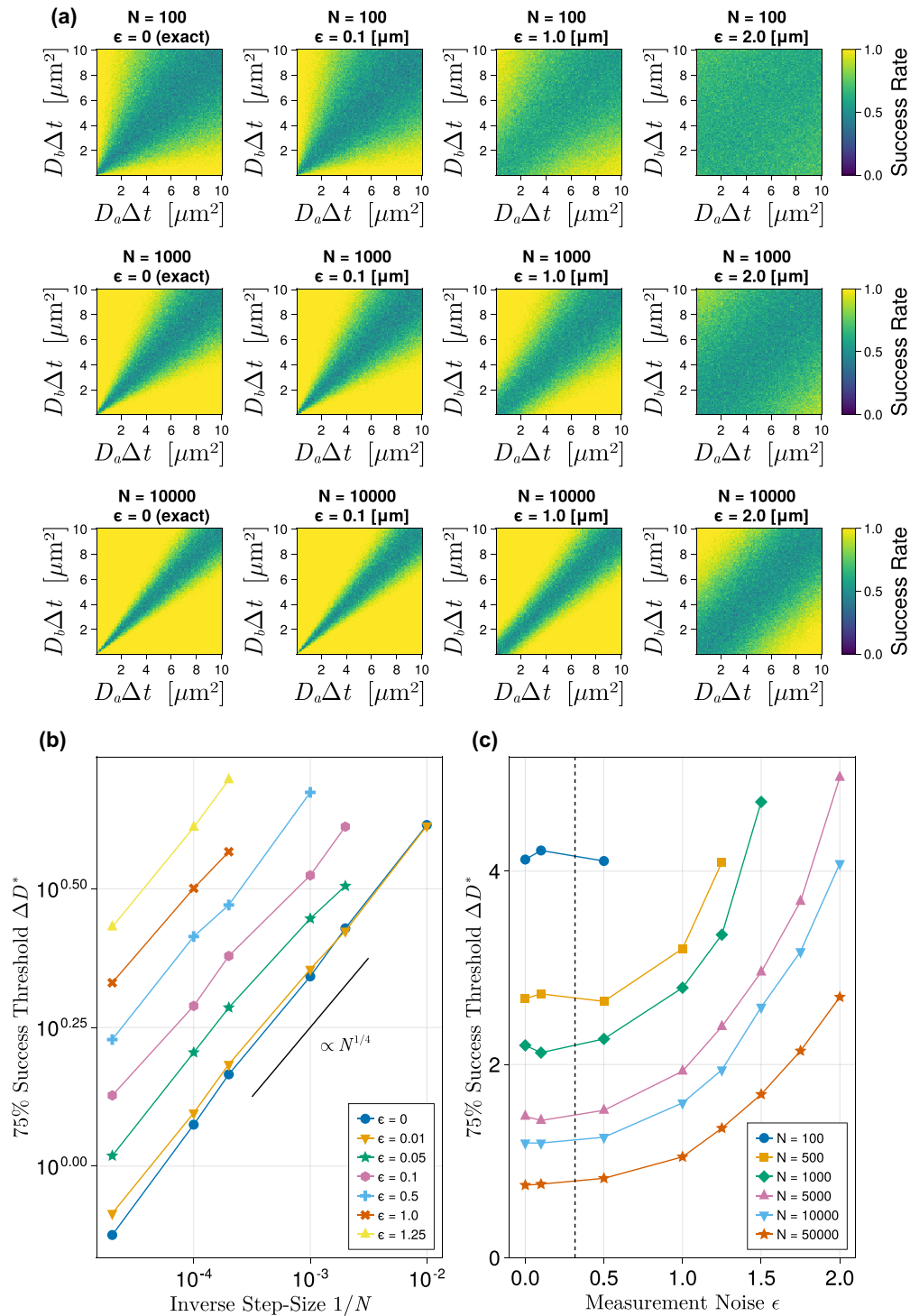


FIG. 7. Influence of trajectory length N and magnitude of measurement noise ϵ on the success rate of anisotropy detection. (a) Heat map of the success rate on the $D_a - D_b$ plane. (b) We define ΔD^* as the width of the interval on $D_a\Delta t + D_b\Delta t = 10.0 \mu\text{m}^2$ on which the success rate is smaller than 75%. The plots indicate that ΔD^* vanishes as $\mathcal{O}(N^{-1/4})$ as N tends to infinity. (c) When the noise magnitude ϵ is smaller than the dashed line (corresponding to ϵ where the signal-to-noise ratio is 1), the measurement noise has little impact on the success rate. However, for ϵ larger than the dashed line, the noise magnitude significantly influences the success rate. (b) and (c) Plots are obtained for $\bar{D} = 10.0 \mu\text{m}^2/\text{s}$ and $\Delta t = 0.01 \text{ s}$.

as long as any type of stochastic approach is used for the estimation. Details of the theoretical analysis of the probability of detecting anisotropy are described in the Supplemental Material [42].

From Fig. 6, we can see that even if the particles are isotropic, anisotropy is falsely detected with a certain probability and vice versa. This is consistent with theoretical analysis shown in Fig. 7, which poses significant challenges

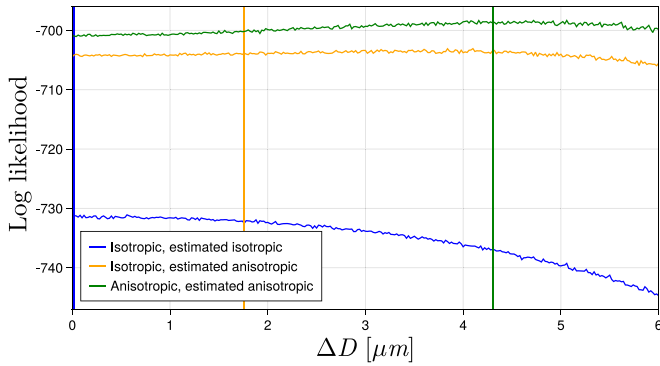


FIG. 8. Typical profiles of the log-likelihood functions in three cases: when a particle is isotropic but is incorrectly estimated to be anisotropic, when it is correctly estimated to be isotropic, and when a particle is anisotropic and correctly estimated to be anisotropic. The vertical lines represent the maximum likelihood estimates in each case. $N = 1000$, $\Delta t = 0.01$ s, and $\epsilon = 0.1$ μm . In the isotropic case $D_a = D_b = 5.0$ $\mu\text{m}^2/\text{s}$, $D_\theta = 100$ rad^2/s and in the anisotropic case $D_a = 7.0$ $\mu\text{m}^2/\text{s}$, $D_b = 3.0$ $\mu\text{m}^2/\text{s}$, $D_\theta = 100$ rad^2/s .

regarding the reliability of the analytical results of experimental data. One possible solution is to use Bayesian inference, which enhances estimation accuracy by introducing a prior distribution to the estimated parameters when prior knowledge is available. Another approach is to examine the profile of the likelihood function. Figure 8 illustrates typical profiles of the likelihood function for three scenarios. One scenario depicts an isotropic particle being mistakenly estimated as anisotropic. The other two scenarios refer to cases where isotropic and anisotropic particles are correctly estimated to be isotropic and anisotropic, respectively. This figure shows that when an isotropic particle is incorrectly estimated to be anisotropic, the likelihood function is much flatter than in the other two correctly estimated cases. This means that the estimation result is much less reliable and one should be very careful when accepting it.

III. DISCUSSION

The main subject of our research is the estimation of diffusion coefficients and the detection of diffusion anisotropy based on an anisotropic diffusion model that does not presuppose angular observations. To this end, we propose an MLE method that uses an EM algorithm. We successfully addressed a complicated system containing unobservables, that is, angles, by employing BP within the EM framework and evaluating the posterior distribution using particle filtering. To the best of our knowledge, our method is the first attempt to utilize BP within the MLE for diffusion estimation problems.

It is noteworthy that our method allows for estimating the unobserved variables based on a single short trajectory. This ability can be leveraged in broad applications: revealing the diffusion modes of molecules interconverting latent states [45,46], and estimating the diffusion parameters of an economical system where it is difficult to prepare homogeneous statistical ensembles.

Modifying some prerequisites of our model expands the scope of our method in more complex diffusive systems. For example, the effect of heterogeneous medium viscosities can be incorporated by replacing the Gaussian distribution of a tracer step Eq. (5) with an exponential-like one [47], which is relevant in a highly heterogeneous intracellular environment. Biological activities around tracers require adding nonthermal fluctuations to Eqs. (5) and (6), or coupling the diffusion equations of a tracer with active background dynamics [48,49]. Extending our method to the system with non-Markov diffusion [50], confined geometries [51], and external fields [52] is also of practical importance and expected in future works.

Using numerical studies and experimental tests, we demonstrated that the MLE method outperforms conventional methods based on MSD and fourth-order cumulants in various parameter regimes. Conventional methods often failed to estimate diffusion coefficients, even with $N > 3000$, whereas our MLE method was successful with as few as $N = 100$ observations. This ensured that our method is applicable to realistic situations in which the macroscopic non-Gaussianity is almost entirely masked owing to high rotational diffusion coefficients.

Moreover, our theoretical analysis revealed that the probability of anisotropy detectability depends on the trajectory length N and measurement noise ϵ . First, we showed that the success of the MLE method lies in its ability to decouple the dependencies between ΔD and D_θ , which are strongly coupled in the fourth-order cumulants. Second, we found that in the limit where D_θ approaches infinity, anisotropy is theoretically always detectable for infinite trajectory lengths, whereas the finiteness of the lengths can sometimes lead to an isotropic solution as the optimal solution. This indicates a theoretical limit for anisotropy detection, quantitatively demonstrating how the lack of observations or the presence of observation noise adversely affects estimation, thereby highlighting the need for improvements to the measurement precision rather than algorithmic enhancements. Thus, this study provides both qualitative and quantitative guidelines for increasing the measurement accuracy.

Finally, a comparison of our outcome with that of recent research [53] on binary classification between anisotropic and isotropic diffusion is of interest. Because the previous study employed deep learning and focused solely on binary classification, the underlying estimation principle was largely a black box, and quantitative estimation of the anisotropic diffusion coefficients remained impossible. In contrast, our results provide a theoretical basis for the limitations of the success probability of estimation, in addition to quantitative and reliable detection.

IV. METHOD

Overview of estimation algorithm

To estimate the diffusion coefficients and detect their anisotropy, instead of the conventional cumulant-based methods, we employed MLE, which has been shown to be useful for estimating diffusion coefficients in much simpler models [12,13,41,54,55] or some specific cases [56,57].

First, Eq. (1) was discretized using Ito's method to convert the diffusion process into a set of stochastic equations as follows:

$$(x_{i+1} - x_i, y_{i+1} - y_i) \sim \mathbf{Norm}(\mathbf{0}, \mathbf{\Sigma}_i \Delta t), \quad (5)$$

$$\theta_{i+1} - \theta_i \sim \mathbf{Norm}(0, 2D_\theta \Delta t), \quad (6)$$

$$X_i \sim \mathbf{Norm}(x_i, \epsilon^2), \quad (7)$$

$$Y_i \sim \mathbf{Norm}(y_i, \epsilon^2), \quad (8)$$

where $\mathbf{\Sigma}_i = \mathbf{\Sigma}(\theta_i)$. From these equations, we derived the following expression for the likelihood function:

$$\begin{aligned} p(\mathbf{X}, \mathbf{Y} | \mathbf{D}) &\propto \int dx dy d\theta \\ &\times \exp\left(-\sum_i \left\{ \frac{1}{4\Delta t} \left(\frac{u_i^2}{D_a} + \frac{v_i^2}{D_b} + \frac{\Delta\theta_i^2}{D_\theta} \right) \right\}\right) \\ &\times \exp\left(-\sum_i \frac{(x_i - X_i)^2 + (y_i - Y_i)^2}{2\epsilon^2}\right), \end{aligned} \quad (9)$$

where $\mathbf{D} = (D_a, D_b, D_\theta)$ and

$$u_i = \cos \theta_i \Delta x_i + \sin \theta_i \Delta y_i \quad (10)$$

$$v_i = \sin \theta_i \Delta x_i - \cos \theta_i \Delta y_i. \quad (11)$$

Our objective was to estimate \mathbf{D} using Eq. (9). This could be performed using the Markov chain Monte Carlo method. However, this approach is not feasible because the transition probabilities of the Markov chain that converge to $p(\mathbf{D} | \mathbf{X}, \mathbf{Y}) \propto p(\mathbf{X}, \mathbf{Y} | \mathbf{D})$ generally scale exponentially with respect to N . This yields huge statistical fluctuations in sampling, which prevents accurate estimation of \mathbf{D} . Therefore, we used the MLE method instead, which is free from the large statistical fluctuations and can be performed using the EM algorithm with $\mathcal{O}(N)$ computational cost per update, as shown below.

The EM algorithm that iterates

$$D_a^{k+1} = \frac{1}{2T} \left\langle \sum_{i=1}^{N-1} (\cos \theta_i \Delta x_i + \sin \theta_i \Delta y_i)^2 \right\rangle_{\mathbf{D}^k} \quad (12)$$

$$D_b^{k+1} = \frac{1}{2T} \left\langle \sum_{i=1}^{N-1} (\sin \theta_i \Delta x_i - \cos \theta_i \Delta y_i)^2 \right\rangle_{\mathbf{D}^k} \quad (13)$$

$$D_\theta^{k+1} = \frac{1}{2T} \left\langle \sum_{i=1}^{N-1} \Delta\theta_i^2 \right\rangle_{\mathbf{D}^k} \quad (14)$$

with the appropriate initial conditions is guaranteed to converge to a local maximum of Eq. (9), where k counts the number of iterations, $\mathbf{D}^k = (\mathbf{D}_a^k, \mathbf{D}_b^k, \mathbf{D}_\theta^k)$, $T = N\Delta t$, and $\Delta x_i = x_{i+1} - x_i$, $\Delta y_i = y_{i+1} - y_i$, $\Delta\theta_i = \theta_{i+1} - \theta_i$. The expectation $\langle \dots \rangle_{\mathbf{D}^k}$ is considered under the posterior distribution $p(\mathbf{x}, \mathbf{y}, \boldsymbol{\theta} | \mathbf{X}, \mathbf{Y}, \mathbf{D}^k)$.

The subsequent step involves computing the expectations on the right-hand side of Eqs. (12)–(14). We perform this using BP [38], which is an efficient algorithm that is applicable to probabilistic models defined over cycle-free graphs. In the

current system, BP propagates auxiliary distributions, termed “messages,” as

$$v_i(\mathbf{z}_i) \propto \int d\mathbf{z}_{i-1} v_{i-1}(\mathbf{z}_{i-1}) p(\mathbf{z}_i | \mathbf{z}_{i-1}) p(x_i, y_i | X_i, Y_i) \quad (15)$$

$$\mu_i(\mathbf{z}_i) \propto \int d\mathbf{z}_{i+1} \mu_{i+1}(\mathbf{z}_{i+1}) p(\mathbf{z}_i | \mathbf{z}_{i+1}) p(x_i, y_i | X_i, Y_i) \quad (16)$$

along a chain that corresponds to a sequence of latent variables $\mathbf{z}_i = (x_i, y_i, \theta_i)$ ($i = 1, \dots, N$) in the forward and backward directions. Once messages $v_i(\mathbf{z}_i)$ and $\mu_i(\mathbf{z}_i)$ have been computed for $i = 1, \dots, N$, the joint posterior distribution can be assessed as

$$p(\mathbf{z}_i, \mathbf{z}_{i+1} | \mathbf{X}, \mathbf{Y}, \mathbf{D}) \propto v_i(\mathbf{z}_i) p(\mathbf{z}_{i+1} | \mathbf{z}_i) \mu_{i+1}(\mathbf{z}_{i+1}), \quad (17)$$

which makes it possible to efficiently compute the right side of Eqs. (12)–(14).

The cost for computing Eqs. (15) and (16) for $i = 1, \dots, N$ scales only linearly with respect to N . However, analytically performing the functional update of the BP remains challenging. To overcome this problem, we used sampling methods known as particle filters or sequential Monte Carlo methods [39,40]. This approach uses a Monte Carlo approximation of the distribution, preserving it as a population of “particles.” Although this induces some Monte Carlo errors and compromises exactness, augmenting the number of particles can lead to improved approximations. Particle degeneracy is an inherent issue in particle filters; however, in our model, adept interweaving of the diffusion-propagation step with the observation-resampling step effectively minimized the problems resulting from degeneracy. The detailed algorithm for preventing degeneracy is described in the Supplemental Material [42].

Calculating the joint distribution Eq. (17) is inherently more challenging than calculating its marginalized counterpart $p(\mathbf{z}_i | \mathbf{X}, \mathbf{Y}, \mathbf{D})$. This occurs because the absence of measured data meant that θ_i and θ_{i+1} sampled from $v_i(\mathbf{z}_i)$ and $\mu_{i+1}(\mathbf{z}_{i+1})$ are almost uncorrelated, yielding large statistical fluctuations when assessing Eq. (17) using naive particle filters. We have addressed the techniques to mitigate this challenge in the Supplemental Material [42]. In particular, D_θ empirically showed extremely slow convergence in the EM algorithm, with convergent solutions often not reaching satisfactory approximations. Thus, by leveraging the efficiency of the particle filter in the likelihood function computation, we exclusively employed surrogate-based optimization [58] to determine the likelihood function when calculating the maximum likelihood value for D_θ . This algorithm allowed for approximate optimization with high precision, even when the objective function exhibited Monte Carlo fluctuations. Finally, an efficient method for computing the likelihood function using a particle filter is described in the Supplemental Material [42].

V. EXPERIMENTS

A. Sample preparation

1. Fluorescent spheres

The fluorescent spheres solution (F-8764, Invitrogen; 2% solids, nominal diameter 200 nm) was diluted 10^4 times

with Milli-Q water. Then, 10 μL of the diluted solution was mounted on a cover glass (No. 1 22×22 mm, Matsunami) and sealed by placing another cover glass on it with a double-sided PET tape of 5 μm thickness (No. 5600, Nitto) as a spacer between the two cover glasses.

2. Quantum rods

The CdSe/CdS core-shell-type quantum rods (900514-1ML, Sigma-Aldrich) were diluted in toluene (204-17915, Wako) at a density of 0.5 $\mu\text{g}/\text{mL}$ and sonicated for 30 min (M1800-J, Branson) to disperse uniformly in suspension. Next, 10 μL of the diluted sample was mounted on a cover glass (No. 1 22×22 mm, Matsunami) and sealed by placing another cover glass on it with a double-sided polyimide tape of 130 μm thickness (Kincsem110-02, HCP) as a spacer. The nominal major and minor axis length of the quantum rod was 28.4 ± 3.0 and 4.6 ± 0.7 nm, respectively.

3. Bacteria

E. coli strain RA1 suspended in buffer (50 mM HEPES, pH 7.0) was first sterilized by heating at 60°C for 45 min to terminate its swimming motion and observe only its pure diffusion. Then, it was mounted on a cover glass (No. 1 24×60 mm, Matsunami). To observe quasi-two-dimensional diffusion of the bacteria, the resulting sample was sealed by placing another cover glass on it, with a double-sided PET tape of 5 μm thickness (No. 5600, Nitto) as the spacer.

B. Microscopy

1. Fluorescent spheres

Imaging of fluorescent microspheres was performed using an inverted microscope (IX83, Olympus) equipped with a 100 \times oil-immersion objective (UPlanSAPO, Olympus), a mercury light source system (U-HGLGPS, Olympus), and a fluorescence filter unit (U-FBNA, Olympus). The images were detected using a sCMOS camera (ORCA Flash4.0, Hamamatsu) at 100 fps with 1152×1152 pixels in 16-bit depth. The image acquisition process was controlled using cellSens (Olympus).

2. Quantum rods

The fluorescent images of quantum rods were captured using an inverted microscope (IX83, Olympus) equipped with a 100 \times oil-immersion objective (UPlanSAPO, Olympus), a mercury light source system (U-HGLGPS, Olympus), and a fluorescence filter unit (U-FGNA, Olympus). The images

were detected using a sCMOS camera (ORCA Flash4.0, Hamamatsu) at 100 fps with 1152×1152 pixels in 16-bit depth. The image acquisition process was controlled using cellSens (Olympus). To track the quantum rods moving in quasi-two dimensions wherever possible, fluorescent spots that were in focus during observation were selected to analyze their trajectories.

3. Bacteria

The transmitted images of bacteria were acquired using an inverted microscope (IX73, Olympus) equipped with a 100 \times oil-immersion objective (UAPON100XOTIRF, Olympus) and transmitted illumination (M660L4, Thorlab). The images were detected using a high-speed camera (FASTCAM NovaS, Photron) at 3000 fps with 1024×1024 pixels in 8-bit depth.

C. Image analysis

For each pixel, a temporal median was first calculated to obtain a background image which only contained tracers immobilized on the cover glass. The background image was then subtracted from each frame of the original image sequences, resulting in an image that only contained mobile tracers. The centroid of each fluorescent sphere and quantum rod at every time point was determined by fitting an isotropic Gaussian profile onto the respective spot image. The centroid and angle of each bacterium were calculated using an anisotropic Gaussian profile instead. The measurement error ϵ was estimated as the positional standard deviation of the tracers immobilized on the glass wall.

The code used in this paper is available from Ref. [59]. All data reported in this paper will be deposited in the public database, Systems Science of Biological Dynamics repository [60].

ACKNOWLEDGMENTS

This work was supported by the Japan Society for the Promotion of Science (JSPS) KAKENHI Grant-in-Aid for Scientific Research on Innovative Areas, “Information Physics of Living Matters” (Grants No. JP19H05794 and No. JP19H05795) to Y.O. and Grant-in-Aid for Transformative Research Areas (A), “Foundation of Machine Learning Physics” (Grant No. JP22H05117) to Y.K., and by the Japan Science and Technology Agency (JST) Grants No. JPMJCR20E2 and No. JPMJMS2025-14 to Y.O., Grants No. JPMJCR20E5 and No. JPMJMS2022-14 to M.K., and Grant No. JPMJCR1912 to Y.K.

[1] C. R. K. Windows-Yule, M. T. Herald, A. L. Nicușan, C. S. Wiggins, G. Pratz, S. Manger, A. E. Odo, T. Leadbeater, J. Pellico, R. T. M. de Rosales, A. Renaud, I. Govender, L. B. Carasik, A. E. Ruggles, T. Kokalova-Wheldon, J. P. K. Seville, and D. J. Parker, Recent advances in positron emission particle tracking: A comparative review, *Rep. Prog. Phys.* **85**, 016101 (2022).

[2] M. J. Saxton and K. Jacobson, Single-particle tracking: Applications to membrane dynamics, *Annu. Rev. Biophys. Biomol. Struct.* **26**, 373 (1997).

[3] C. Manzo and M. F. Garcia-Parajo, A review of progress in single particle tracking: From methods to biophysical insights, *Rep. Prog. Phys.* **78**, 124601 (2015).

[4] Z. Wang, X. Wang, Y. Zhang, W. Xu, and X. Han, Principles and applications of single particle tracking in cell research, *Small* **17**, 2005133 (2021).

[5] Y. Liao, Y. Li, J. W. Schroeder, L. A. Simmons, and J. S. Biteen, Single-molecule DNA polymerase dynamics at a bacterial replisome in live cells, *Biophys. J.* **111**, 2562 (2016).

- [6] Y. Ma, G. Mao, G. Wu, and X.-E. Zhang, Single-particle tracking reveals the interplay between HIV-1 reverse transcription and uncoating, *Anal. Chem.* **94**, 2648 (2022).
- [7] T. T. Yang, M. N. T. Tran, W. M. Chong, C.-E. Huang, and J.-C. Liao, Single-particle tracking localization microscopy reveals nonaxonemal dynamics of intraflagellar transport proteins at the base of mammalian primary cilia, *Mol. Biol. Cell* **30**, 828 (2019).
- [8] D. Holcman, P. Parutto, J. E. Chambers, M. Fantham, L. J. Young, S. J. Marciniak, C. F. Kaminski, D. Ron, and E. Avezov, Single particle trajectories reveal active endoplasmic reticulum luminal flow, *Nat. Cell Biol.* **20**, 1118 (2018).
- [9] Y. Cui, M. Yu, X. Yao, J. Xing, J. Lin, and X. Li, Single-particle tracking for the quantification of membrane protein dynamics in living plant cells, *Mol. Plant* **11**, 1315 (2018).
- [10] S.-L. Liu, Z.-G. Wang, H.-Y. Xie, A.-A. Liu, D. C. Lamb, and D.-W. Pang, Single-virus tracking: From imaging methodologies to virological applications, *Chem. Rev.* **120**, 1936 (2020).
- [11] J. Liu, M. Xu, B. Tang, L. Hu, F. Deng, H. Wang, D.-W. Pang, Z. Hu, M. Wang, and Y. Zhou, Single-particle tracking reveals the sequential entry process of the bunyavirus severe fever with thrombocytopenia syndrome virus, *Small* **15**, 1803788 (2019).
- [12] J. T. Bullerjahn and G. Hummer, Maximum likelihood estimates of diffusion coefficients from single-particle tracking experiments, *J. Chem. Phys.* **154**, 234105 (2021).
- [13] Y. Lin and S. B. Andersson, Expectation maximization based framework for joint localization and parameter estimation in single particle tracking from segmented images, *PLoS One* **16**, e0243115 (2021).
- [14] S. S. Pradhan and S. Saha, Advances in design and applications of polymer brush modified anisotropic particles, *Adv. Colloid Interface Sci.* **300**, 102580 (2022).
- [15] L. Cai, F. Bian, H. Chen, J. Guo, Y. Wang, and Y. Zhao, Anisotropic microparticles from microfluidics, *Chem* **7**, 93 (2021).
- [16] A. K. Pearce, T. R. Wilks, M. C. Arno, and R. K. O'Reilly, Synthesis and applications of anisotropic nanoparticles with precisely defined dimensions, *Nat. Rev. Chem.* **5**, 21 (2021).
- [17] I. Mirza and S. Saha, Biocompatible anisotropic polymeric particles: Synthesis, characterization, and biomedical applications, *ACS Appl. Bio Mater.* **3**, 8241 (2020).
- [18] R. A. Meyer and J. J. Green, Shaping the future of nanomedicine: Anisotropy in polymeric nanoparticle design: Shaping the future of nanomedicine, *Wiley Interdiscip. Rev. Nanomed. Nanobiotechnol.* **8**, 191 (2016).
- [19] W. L. Lee, Y. C. Seh, E. Widjaja, H. C. Chong, N. S. Tan, and S. C. J. Loo, Fabrication and drug release study of double-layered microparticles of various sizes, *J. Pharm. Sci.* **101**, 2787 (2012).
- [20] L. Yang, Z. Zhou, J. Song, and X. Chen, Anisotropic nanomaterials for shape-dependent physicochemical and biomedical applications, *Chem. Soc. Rev.* **48**, 5140 (2019).
- [21] D. Kargari Aghmiouni and S. Khoei, Dual-drug delivery by anisotropic and uniform hybrid nanostructures: A comparative study of the function and substrate-drug interaction properties, *Pharmaceutics* **15**, 1214 (2023).
- [22] S. E. Moran, I. R. Bruss, P. W. A. Schönhöfer, and S. C. Glotzer, Particle anisotropy tunes emergent behavior in active colloidal systems, *Soft Matter* **18**, 1044 (2022).
- [23] R. Förth, Die brownsche bewegung bei berücksichtigung einer persistenz der bewegungsrichtung. Mit anwendungen auf die bewegung lebender infusorien, *Z. Phys.* **2**, 244 (1920).
- [24] F. Perrin, Mouvement brownien d'un ellipsoïde - I. dispersion diélectrique pour des molécules ellipsoïdales, *J. Phys. Radium* **5**, 497 (1934).
- [25] F. Perrin, Mouvement Brownien d'un ellipsoïde (II). Rotation libre et dépolariation des fluorescences. Translation et diffusion de molécules ellipsoïdales, *J. Phys. Radium* **7**, 1 (1936).
- [26] Y. Han, A. M. Alsayed, M. Nobili, J. Zhang, T. C. Lubensky, and A. G. Yodh, Brownian motion of an ellipsoid, *Science* **314**, 626 (2006).
- [27] C. Ribault, A. Triller, and K. Sekimoto, Diffusion trajectory of an asymmetric object: Information overlooked by the mean square displacement, *Phys. Rev. E* **75**, 021112 (2007).
- [28] S. Roh, J. Yi, and Y. W. Kim, Analysis of diffusion trajectories of anisotropic objects, *J. Chem. Phys.* **142**, 214302 (2015).
- [29] I. Hanasaki and Y. Isono, Detection of diffusion anisotropy due to particle asymmetry from single-particle tracking of Brownian motion by the large-deviation principle, *Phys. Rev. E* **85**, 051134 (2012).
- [30] M. Yoshida, S. Miyazaki, and H. Fujisaka, Irregular parameter dependence of generalized diffusion coefficients based on large deviation statistical analysis, *Phys. Rev. E* **74**, 026204 (2006).
- [31] M. A. Charsooghi, E. A. Akhlaghi, S. Tavaddod, and H. R. Khalesifard, A MATLAB program to calculate translational and rotational diffusion coefficients of a single particle, *Comput. Phys. Commun.* **182**, 400 (2011).
- [32] H. Qian, M. P. Sheetz, and E. L. Elson, Single particle tracking. analysis of diffusion and flow in two-dimensional systems, *Biophys. J.* **60**, 910 (1991).
- [33] L. Weimann, K. A. Ganzinger, J. McColl, K. L. Irvine, S. J. Davis, N. J. Gay, C. E. Bryant, and D. Klenerman, A quantitative comparison of single-dye tracking analysis tools using Monte Carlo simulations, *PLoS One* **8**, e64287 (2013).
- [34] D. Ernst and J. Kühler, Measuring a diffusion coefficient by single-particle tracking: Statistical analysis of experimental mean squared displacement curves, *Phys. Chem. Chem. Phys.* **15**, 845 (2013).
- [35] M. J. Saxton, Single-particle tracking: The distribution of diffusion coefficients, *Biophys. J.* **72**, 1744 (1997).
- [36] C. L. Vestergaard, P. C. Blainey, and H. Flyvbjerg, Optimal estimation of diffusion coefficients from single-particle trajectories, *Phys. Rev. E* **89**, 022726 (2014).
- [37] A. P. Dempster, N. M. Laird, and D. B. Rubin, Maximum likelihood from incomplete data via the EM algorithm, *J. R. Stat. Soc. Series B Stat. Methodol.* **39**, 1 (1977).
- [38] J. Pearl, *Probabilistic Reasoning in Intelligent Systems: Networks of Plausible Inference* (Morgan Kaufmann, Oxford, 1997).
- [39] G. Kitagawa, Monte Carlo filter and smoother for non-Gaussian nonlinear state space models, *J. Comput. Graph. Stat.* **5**, 1 (1996).
- [40] J. S. Liu and R. Chen, Sequential Monte Carlo methods for dynamic systems, *J. Am. Stat. Assoc.* **93**, 1032 (1998).

- [41] D. Boyer, D. S. Dean, C. Mejía-Monasterio, and G. Oshanin, Optimal estimates of the diffusion coefficient of a single Brownian trajectory, *Phys. Rev. E* **85**, 031136 (2012).
- [42] See Supplemental Material at <http://link.aps.org/supplemental/10.1103/PhysRevResearch.6.033272> for additional details on the estimation method based on statistical measures, a detailed description of the EM algorithm, fixed point analysis of the EM algorithm, characterization of the failure solution, bright field movie of a diffusing bacterium, fluorescent movie of a quantum rod, and fluorescent movie of a sphere.
- [43] J. L. Bitter, Y. Yang, G. Duncan, H. Fairbrother, and M. A. Bevan, Interfacial and confined colloidal rod diffusion, *Langmuir* **33**, 9034 (2017).
- [44] J. Rudnick and G. Gaspari, The asphery of random walks, *J. Phys. A: Math. Gen.* **19**, L191 (1986).
- [45] C. Dieball, D. Krapf, M. Weiss, and A. Godec, Scattering fingerprints of two-state dynamics, *New J. Phys.* **24**, 023004 (2022).
- [46] A. Sabri, X. Xu, D. Krapf, and M. Weiss, Elucidating the origin of heterogeneous anomalous diffusion in the cytoplasm of mammalian cells, *Phys. Rev. Lett.* **125**, 058101 (2020).
- [47] N. A. Bustos, C. M. Saad-Roy, A. G. Cherstvy, and C. E. Wagner, Distributed medium viscosity yields quasi-exponential step-size probability distributions in heterogeneous media, *Soft Matter* **18**, 8572 (2022).
- [48] Y. Peng, L. Lai, Y.-S. Tai, K. Zhang, X. Xu, and X. Cheng, Diffusion of ellipsoids in bacterial suspensions, *Phys. Rev. Lett.* **116**, 068303 (2016).
- [49] J. Shin, A. G. Cherstvy, W. K. Kim, and V. Zaburdaev, Elasticity-based polymer sorting in active fluids: A Brownian dynamics study, *Phys. Chem. Chem. Phys.* **19**, 18338 (2017).
- [50] D. Boyer, D. S. Dean, C. Mejía-Monasterio, and G. Oshanin, Ergodic least-squares estimators of the generalized diffusion coefficient for fractional Brownian motion, *Phys. Rev. E* **87**, 030103(R) (2013).
- [51] A. G. Godin, J. A. Varela, Z. Gao, N. Danné, J. P. Dupuis, B. Lounis, L. Groc, and L. Cognet, Single-nanotube tracking reveals the nanoscale organization of the extracellular space in the live brain, *Nat. Nanotechnol.* **12**, 238 (2017).
- [52] M. Dessard, J.-B. Manneville, and J.-F. Berret, Cytoplasmic viscosity is a potential biomarker for metastatic breast cancer cells, *Nanoscale Adv.* **6**, 1727 (2024).
- [53] H. Fukuda, H. Kuramochi, Y. Shibuta, and T. Ichiki, Analysis of Brownian motion trajectories of non-spherical nanoparticles using deep learning, *APL Mach. Learn.* **1**, 046104 (2023).
- [54] B. Shuang, C. P. Byers, L. Kisley, L.-Y. Wang, J. Zhao, H. Morimura, S. Link, and C. F. Landes, Improved analysis for determining diffusion coefficients from short, single-molecule trajectories with photoblinking, *Langmuir* **29**, 228 (2013).
- [55] G. Makkai, I. M. Abraham, K. Barabas, S. Godo, D. Ernszt, T. Kovacs, G. Kovacs, S. Szocs, and T. Z. Janosi, Maximum likelihood-based estimation of diffusion coefficient is quick and reliable method for analyzing estradiol actions on surface receptor movements, *Front. Neuroinform.* **17**, 1005936 (2023).
- [56] K. R. Haas, H. Yang, and J.-W. Chu, Expectation-maximization of the potential of mean force and diffusion coefficient in Langevin dynamics from single molecule FRET data photon by photon, *J. Phys. Chem. B* **117**, 15591 (2013).
- [57] P. K. Koo, M. Weitzman, C. R. Sabanaygam, K. L. van Golen, and S. G. J. Mochrie, Extracting diffusive states of Rho GTPase in live cells: Towards in vivo biochemistry, *PLoS Comput. Biol.* **11**, e1004297 (2015).
- [58] M. Urquhart, E. Ljungskog, and S. Sebben, Surrogate-based optimisation using adaptively scaled radial basis functions, *Appl. Soft Comput.* **88**, 106050 (2020).
- [59] <https://github.com/taka255/AnisotropicDiffusionEstimate>.
- [60] <https://ssbd.riken.jp/repository/>.